Talanta 119 (2014) 385–395

Contents lists available at ScienceDirect

Talanta

journal homepage: www.elsevier.com/locate/talanta

Rapid and non-invasive quantification of intramuscular fat content of intact pork cuts

H. Huang [a], L. Liu [a], M.O. Ngadi [a,*], C. Gariépy [b]

[a] Department of Bioresource Engineering, McGill University, Macdonald Campus. 21,111 Lakeshore Road, Ste-Anne-de-Bellevue, Quebec, Canada H9X 3V9
[b] Agriculture and Agri-food Canada, 3600 Casavant West, Saint-Hyacinthe, Quebec, Canada J2S 8E3

ARTICLE INFO

Article history:
Received 10 August 2013
Received in revised form
5 November 2013
Accepted 5 November 2013
Available online 12 November 2013

Keywords:
Intramuscular fat content
Gabor filter
Gray level co-occurrence matrix
Partial least squares regression
Multiple linear regression
Distribution map

ABSTRACT

Having acquired near infrared (NIR) hyperspectral images of intact pork loin samples through an NIR hyperspectral imaging system, the efficiency of a variety of image processing techniques including texture pattern analysis techniques were applied to process hyperspectral images so as to determine the intramuscular fat (IMF) content non-destructively. After the segmentation of region of interest (ROI), the raw spectral, texture-based spectral and textural characteristics of pork images were extracted by spectral averaging and pattern recognition techniques namely Gabor filter and improved gray level co-occurrence matrix (GLCM), respectively. First derivatives of the non-filtered and the Gabor filtered spectra were also investigated. Full waveband partial least squares regression (PLSR) was employed to determine the optimal parameters of Gabor filter and GLCM, and to select optimal wavelengths for IMF prediction. A stepwise procedure was applied to the optimal wavelengths to further optimize them to key wavelengths. Multiple linear regression (MLR) models were built based on the key wavelengths. Mean spectra and the Gabor filtered spectra outperformed GLCM. The best result, represented by correlation coefficients of calibration (*Rc*), cross validation (*Rcv*) and prediction (*Rp*) of 0.89, 0.89, and 0.86, respectively, was achieved using the first derivative of Gabor filtered spectra at 1193 and 1217 nm. To visualize the IMF content in pork, the distribution maps of IMF content in pork were drawn using a mean spectra-based MLR model. These promising results highlight the great potential of NIR hyperspectral imaging for non-destructive prediction of IMF content of intact pork.

1. Introduction

Intramuscular fat (IMF) refers to the fat deposited inside a piece of muscle, so accordingly intramuscular fat content is defined as the mass of IMF, including the visible fat and the non-visible fat in the muscle cell. IMF content influences the cooking quality of pork (flavor, juiciness, etc.), eating satisfaction of consumers, and even health-related issues. Thus, different levels of IMF content can lead to different levels of consumer acceptance [1,2]. Non-invasive and rapid determination of IMF content of pork chops would allow commercial cuts to be classified, screened, and assigned to a proper retail category according to different market targets, thereby enhancing their market allocation and reducing handling costs. At present, the assessment of IMF content of pork involves solvent-based lipid extraction, which is a time consuming, labor intensive and environmentally harmful process. Since chemical extraction-based IMF prediction is not suitable for fast and non-destructive assessment of IMF content of pork, random sampling is typically used in the evaluation of IMF content of pork products. As this leads to non-optimal grading of pork cuts, it would be beneficial to the pork industry to develop a non-destructive, real-time, rapid, and accurate method for predicting IMF content of pork.

Studies have been conducted to evaluate IMF content of pork meat through spectroscopic means [3–7]. Savenije et al. [6] applied a near infrared (NIR) reflectance spectrophotometer to the determination of IMF content of meat obtained from three contrasting breeds. The second derivative of the reflected spectra was used to build prediction models. Correlation coefficients of calibration (*Rc*) between the measured and predicted IMF contents ranged from 0.70 to 0.86, while correlation coefficients of validation (*Rv*) ranged from 0.63 to 0.76. Prevolnik et al. [4] and Barlocco et al. [5] found that estimate of IMF levels by NIR spectroscopy were more accurate when derived from minced pork muscle other than intact pork muscle, highlighting the limitations of spectroscopic

Abbreviations: **DMG**, the first derivative of Gabor-filtered mean spectra; **DMS**, the first derivative of non-filtered mean spectra; GF, Gabor filter; **GIa**, angular second moment of GLCM; **GIh**, homogeneity; **GIt**, contrast of GLCM; **Gin**, correlation of GLCM; **MG**, Gabor-filtered mean spectra; **MS**, non-filtered mean spectra; **WLD**, wide line detector.

* Corresponding author. Tel.: +1 514 3987779; fax: +1 514 3988387.
E-mail address: michael.ngadi@mcgill.ca (M.O. Ngadi).

0039-9140/$ - see front matter © 2013 Elsevier B.V. All rights reserved.
http://dx.doi.org/10.1016/j.talanta.2013.11.015

technique for determination of IMF content of pork. Given the confined detected area of the spectroscopic system, and the heterogeneous distribution of fat in pork muscle, only limited information could be obtained. Therefore, to obtain sufficient data from pork samples either destructive homogenization of samples or repetition of spectroscopy-based evaluation is required.

In the face of these limitations, the emerging technique of hyperspectral imaging was exploited to inspect pork quality [8–12]. By integrating both conventional spectroscopy techniques with imaging techniques and enlarging the detection field, hyperspectral imaging overcomes the limitations of spectroscopy, making it possible to identify the spectral details of different chemical components at specified locations in a product [13,14]. From the resultant data cube (*hypercube*), image parameters or spectra can be extracted and analyzed in order to determine the chemical attributes or physical properties of the tested object. Moreover, the hypercube can be stored for further analysis. In addition, no sample preparation is needed to apply hyperspectral imaging. Considering the great potential of this technology, there has been mounting interest in applying hyperspectral imaging to pork quality control [15].

Qiao et al. [9] introduced visible (VIS)/near-infrared (NIR) hyperspectral imaging to classify pork quality and assess pork marbling objectively. Image processing approach namely gray level co-occurrence matrix (GLCM) was adopted to grade pork samples into different meat quality categories classification results of 75–80% were achieved. Liu et al. [10] developed a Gabor filter-based hyperspectral imaging system to grade pork samples into the same meat quality categories. The work obtained a classification accuracy of $84 \pm 1\%$, which improved the earlier result of Qiao et al. [9] by 4%. This implied that effective pattern recognition techniques would enhance the ability of hyperspectral imaging for assessment of pork quality. Promising results in these studies again emphasized the capacity of hyperspectral imaging as the basis for prediction of pork quality attributes.

The functional bonds of C–H and O–H in fat are closely linked to some frequencies in the NIR region, accounting for why the use of NIR hyeprspectral imaging for IMF content prediction might produce better results than hyeprspectral imaging in the visible (VIS) region. Kobayashi et al. [16] and Wold et al. [17] successfully applied NIR hyperspectral imaging for control of fat content in beef. However, hyperspectral imaging of pork presents a greater challenge, compared to beef, due to the lower contrast between fat and lean in pork and the spectral overlaps in the NIR region exhibited by the main constituents of meat (lipid, water, and protein) [19,20]. Nonetheless, Liu et al. [18] reported the use of the hyperspectral imaging technique to predict the IMF content of pork. The reflected images in a specific wavelength interval were accumulated to enhance the contrast between the fat and the non-fat areas. A feature detection method namely the wide line detector then served to detect fat flecks of pork, yielding a prediction accuracy of 0.91 through a linear regression modeling. While this study indicated the possibility of rapid assessment of the intramuscular fat content of pork using NIR hyperspectral imaging, the authors mentioned the need for more sample measurements and wavelength optimization.

The aim of the present study was to investigate the potential of NIR hyperspectral imaging (900–1700 nm) for quantification of IMF content in pork. For this purpose, normal averaging of spectra and two texture pattern techniques namely Gabor filter and improved GLCM were investigated in terms of their ability to draw useful information from NIR spectral images. Partial least squares regression (PLSR) in the whole wave range was used to select feature wavelengths, after which a stepwise procedure was used to further reduce the dimension of optimal wavelengths. The distribution of IMF content of pork was visualized using the built optimal multiple linear regression model.

2. Experimental section

2.1. Sample collection and determination of IMF content

Pork samples from *longissimus* thoracis muscle were collected from the carcasses of 83 pigs which were raised on a local farm. No differing treatment was applied to the animals. To increase the variability in IMF content in the *longissimus* muscle, carcasses showing large differences in back fat thickness between the 3rd/4th last ribs were selected for dissection. At 24 h post-mortem, thin pork slices at the 3rd/4th last thoracic rib of the *longissimus dorsi* (LD) were collected for determination of IMF content. Concurrently, loin chops with 2–2.5 cm in thickness were dissected from the same anatomical location (the 3rd/4th last thoracic rib), individually wrapped in vacuum packs, and transported to the Hyperspectral Imaging Laboratory, McGill University, Montreal, QC, Canada for image acquisition. The shipping was conducted at 4 °C.

Peripheral fat and surrounding muscle were removed from the thin pork slices. The remaining trimmed muscles were ground. The fresh weight based IMF content of the minced fresh pork was measured using ethanol and dichloromethane-based Soxtec extraction [21]. These IMF contents served as reference values for corresponding loin samples.

2.2. NIR hyperspectral imaging system

An NIR hyperspectral imaging system (Fig. 1) was used to capture NIR images of pork loins. The system consisted of an InGaAs camera (XenICs, Belgium), a spectrograph (Headwall photonics, USA, 900–1700 nm), a conveyer (Donner 2200 series, Donner Mfg. Corp., USA), a real-time control motor (MDIP22314, Intelligent motion system Inc., USA), two 50 W tungsten halogen lamps (vertically 25 cm, and horizontally 8 cm away from the samples), a supporting frame, and a computer. Incident illumination was at an angle of 45° to the sample. The distance between lens and the sample was 40 cm. The directions of the lamps were set up to make sure that the light sources are enabled in every part of the sample. Software for data acquisition and conveyer control was installed on the computer (Hyperspec, Headwall Photonics Inc., USA). The system was run at a room temperature (20–25 °C).

The line-scanning pushbroom system employed was operated in a reflectance mode. With the conveyer moving at a predefined speed, the sample was scanned line by line and the reflected light from samples was quantified at wavelengths ranging from 900 to 1700 nm by the spectrograph. A three-dimensional *hypercube* was formed by combining spatial information from the InGaAs camera and spectral information from the spectrograph. The spectral resolution for the system was 4.8 nm while the spatial resolution was roughly 0.6 mm. The spectral dimension covered 167 bands. The number of pixels covered by one spatial dimension was determined by the morphological size of the detected object. The generated *hypercube* was saved in a band-interleaved-by-line (BIL) format, from which NIR images and spectra for each pixel could easily be extracted.

2.3. Image acquisition and calibration

No sample preparation was needed before image acquisition. Each sample was taken out of the refrigerator (4 °C), scanned for few seconds to collect images, and put back to the refrigerator right after the image collection. Considering the distance between light source and the sample, and the speed of image acquisition, the temperature of the sample was assumed to remain nearly at 4 °C and no significant changes occurred to the sample during imaging. Prior to the collection of hyperspectral images from the 2–2.5 cm thick loin chops, dark and white reference images were captured to correct error caused by dark current of the system and

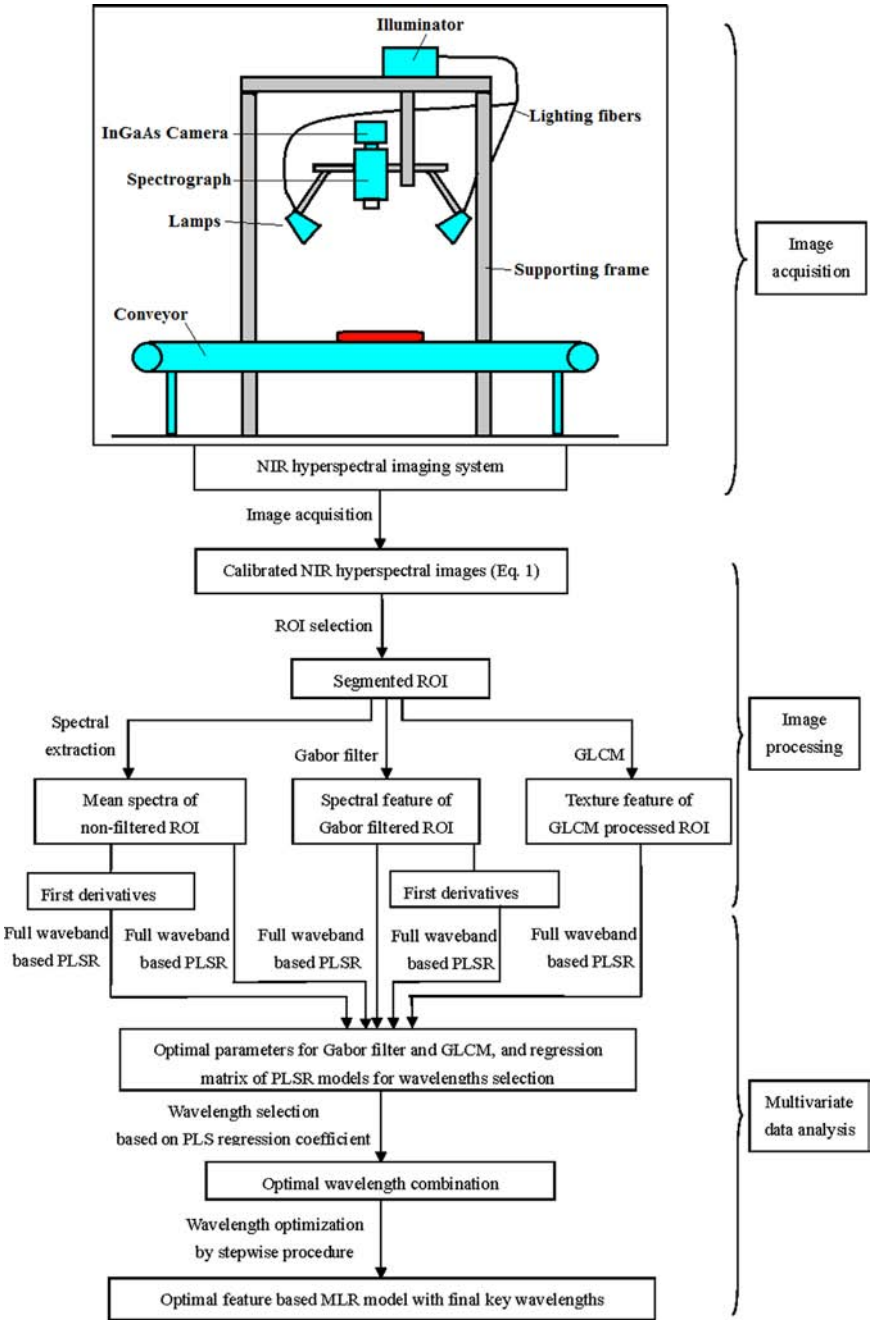

Fig. 1. Flow chart of data acquisition and analysis.

to transform the reflected light intensity to reflectance. The dark image (**D**, with reflectance ~0%) was obtained by covering the lens with an opaque cap. The white reference (**W**, with reflectance ~99%) was obtained by adopting a ceramic tile as photographed object. Original NIR images (N_0) of samples were collected by placing sample on a dark board whose reflectance was close to 0%. Image acquisition of each sample took approximately 4 s. Corrected NIR images (**N**) were obtained by algebraic calculus (Eq. (1)) of the light intensities of each pixel {i, j} in dark (**D**(i, j)), white (**W**(i, j)) and original NIR images (N_0(i, j)). The reflectance of pixels in the calibrated NIR images ranges from 0 to 1. Subsequent image and data analysis (Fig. 1) were conducted using the corrected *hypercube*.

$$N(i,j) = \frac{N_0(i,j) - D(i,j)}{W(i,j) - D(i,j)} \quad (1)$$

2.4. Image processing

The spectral averaging-based and pattern technique-assisted image processing and subsequent multivariate statistical analysis are summarized in Fig. 1. Given the excessive noise of images at 900–935 nm and 1655–1700 nm, only those images obtained over the range of 940–1650 nm were used for image analysis, starting with image preprocessing. All operations of image processing and multivariate statistical analysis in this study were performed using MATLAB 7.3.0 (The MathWorks, Inc., Mass., USA).

2.4.1. Image preprocessing

Regions of interest (ROI) were segmented, from which the spectral and texture features were extracted. ROI Segmentation with the aim of isolating the targeted lean and IMF portion of the

meat from other portions is an important step in image processing, as the selected ROI will affect all further analysis. The peripheral fat, surrounding muscle, shadows and other backgrounds were removed and replaced by a homogenous black background. ROI segmentation in this study was conducted according to the method presented in Liu et al. [22]. The threshold value was automatically set according to the mean and standard deviation of reflectance of each image.

2.4.2. Extraction of spectral feature

The mean spectrum of non-filtered ROI (**MS**) was extracted after image preprocessing. **MS** of each sample was a 1×149 (the wave range/the spectral resolution of the system+1) vector. Average spectra of the two sides of each pork sample were used as final spectral features. In general, there were over 40,000 pixels in the ROI obtained by hyperspectral imaging, hence the error introduced by subjective selection of ROI was reduced comparing to spectroscopy. To raise the ratio of signal to noise, the first derivative (Eq. (2)) was applied to the obtained non-filtered mean spectra. The resulted first derivative of mean spectra (**DMS**) was used for data analysis as well as **MS. DMS** of each pork sample was a 1×148 vector (the wave range/the spectral resolution of the system).

$$D_i = \frac{MS_{i+1} - MS_i}{\lambda_{i+1} - \lambda_i} \tag{2}$$

where i represents the number of wavelengths, $i = 1, 2, 3, \ldots 148$. D_i is the first differential of the mean spectrum at ith wavelength. λ_i is the ith wavelength, with an interval of 4.8 nm between λ_i and λ_{i+1}. MS_{i+1} and MS_i are the value of spectral response at the $(i+1)$ th and ith wavelength, respectively.

2.4.3. Extraction of texture spectrum by Gabor filter

Proposed as an analogue of human vision [10,23], texture pattern technique Gabor filter served to extract texture features from NIR images. The two-dimensional Gabor filter is a transformation of elliptic Gaussian and sinusoidal waves, which are applied on all receptive fields in the image. Gabor filter is capable of extracting the important spatial characteristics including spatial localization and spatial frequency from images. Considering IMF as spatial characteristics in pork images, an isotropic Gabor filter (GF1, Eq. (3)) and an oriented Gabor filter (GF2, Eq. (4)) were used to process pork images at wavelengths ranging from 940 to 1650 nm [24].

$$GF1(x,y,f,\sigma) = \frac{1}{2\pi\sigma^2}\exp\left\{-\frac{x^2+y^2}{2\sigma^2}\right\}\cos\left[2\pi f\left(\sqrt{x^2+y^2}\right)\right] \tag{3}$$

$$GF2(x,y,f,\sigma,\theta) = \frac{1}{2\pi\sigma^2}\exp\left\{-\frac{x^2+y^2}{2\sigma^2}\right\}\cos\left[2\pi f(x\cos\theta + y\sin\theta)\right] \tag{4}$$

where (x, y) are the coordinates of a specified pixel in a given NIR image, f represents the frequency of the sinusoidal wave, σ is the standard deviation of the Gaussian function, and θ is a vector which controls the orientation of the filter ($\theta = 0°, 45°, 90°, 135°$). Since GF1 is an isotropic function, θ was not considered as a parameter for GF1. After filtering, the mean spectral response of the Gabor filtered ROI was obtained. To reduce the influence of heterogeneity in the pork sample, the average spectrum from two surfaces of each sample was obtained and used for subsequent analysis. Mean spectra from GF1 and GF2 processed images were denoted as **MG1** and **MG2**, respectively. The first derivatives of **MG1** and **MG2** were calculated according to Eq. (2) and denoted as **DMG1** and **DMG2**, respectively. **DMG** stands for the first derivatives of both types of Gabor filtered spectra.

2.4.4. Extraction of texture features by improved GLCM

Another texture pattern analysis technique termed gray-level co-occurrence matrix (GLCM) was investigated for processing of hyperspectral images. GLCM provides information about how often the pixel intensities occur between two pixels that are distributed by a specific distance and direction. Features derived by GLCM have been widely used in texture analysis for food quality and safety control [25–27]. In applying GLCM, the subjective selection of a regular shape (e.g. a circle area) is usually used to select the appropriate ROI [9,26]. However, as bias would be introduced by manual interference, especially for heterogeneous objects such as meat products. In the present, an advanced GLCM was applied to the full irregularly shaped ROI of pork loin to avoid the effect of subjective ROI selection.

To calculate texture features, a multi-scale GLCM matrix was derived from each image. For instance, Fig. 2(a) illustrates how an 8-level GLCM matrix was calculated from a 6×5 matrix (i.e. 6×5 image). As the shadow elements shown in Fig. 2(a), with an offset direction of east (0°) and an offset distance of 1.0 between two pixels, two instances of two neighboring pixels having values of 1 and 3 occurred. Hence, the element {1, 3} in the GLCM contains the value 2. The size of the generated GLCM matrix depends on the number of gray scales considered. Usually, eight scales were considered, resulting in an 8×8 square GLCM matrix.

Eight scale levels, four offset directions (Fig. 2(b), 0°, 45°, 90°, 135°), and 11 offset distances between 1 and 3–30 pixels, with a stepsize of three pixels were tried in generating the GLCM matrices. The minimum and the maximum intensities of the input image delimited the scale, which was divided into eight equal levels. For each image, 52 (4 directions × 13 steps=52) different matrices were generated. The image texture features (**GI**) included four measurements calculated from obtained GLCM matrix (Eqs. (5)–(8)): *contrast* (**GIt**), *correlation* (**GIn**), *angular second moment* (ASM, **GIa**), and *homogeneity* (**GIh**)), respectively.

$$Contrast = \sum_{i,j}(i-j)^2 M_{D,\theta}(i,j) \tag{5}$$

$$Correlation = \frac{\sum_{i,j}(ij)M_{D,\theta}(i,j) - \mu_i\mu_j}{\sigma_i\sigma_j} \tag{6}$$

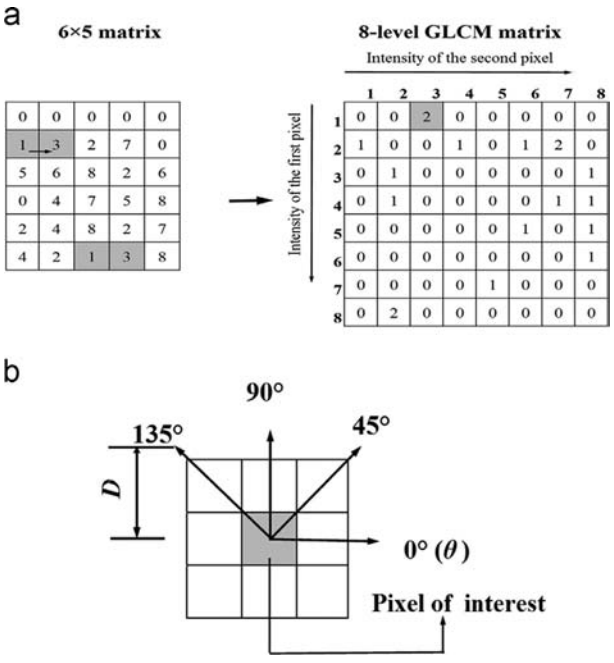

Fig. 2. Principle of GLCM matrix. (a) Form of 8-level GLCM matrix and (b) distibution of pixel pair.

$$ASM = \sum_{i,j}[M_{D,\theta}(i,j)]^2 \quad (7)$$

$$Homogeneity = \sum_{i,j}\frac{M_{D,\theta}(i,j)}{1+(i-j)^2} \quad (8)$$

where (i, j) is the coordination of the pixel of interest, D is the given distance between two pixels, θ is the offset direction of the pair of pixels over an image (θ= 0°, 45°, 90°, 135°), $M_{D,\theta}$ is the obtained GLCM matrix, $M_{D,\theta}(i,j)$ is the value in element $\{i, j\}$ of $M_{D,\theta}$, (μ_i,μ_j) are the means of $M_{D,\theta}(i,j)$ in the row and column directions, and (σ_i,σ_j) are the standard deviations of $M_{D,\theta}(i,j)$ in the row and column directions. As a result, 208 (52 × 4=208) plots with different parameters (θ, D, measurement) were developed from each image. The four measurements of GLCM each served as a type of image texture feature index in the estimation of IMF content of pork.

2.5. Multivariate data analysis

Partial linear square regression (PLSR) and a stepwise procedure were employed in building calibration models, which served in determining optimal parameters for GF and GLCM and key wavelengths for modeling. PLSR method is widely used to reduce the dimensionality of predictor variables and random noise, and has proved to be efficient [7]. In practice, the essential step of PLSR analysis is selecting the number of the main PLS principal components (PLS-PC) which explain the maximum fundamental relations between predict and response variables. After quantification of PLS-PC, the PLSR model is built. The parameters of GF (f, σ, θ) and GLCM (D, θ, measurement), which provided best prediction results in PLSR models, were used as the optimal parameters. The corresponding regression coefficient was used to select optimal wavelengths.

In this study, features at all wavebands (940–1650 nm) were used for the PLSR analysis. The total 83 samples were divided into two sets, including calibration sets (56 samples) and prediction sets (27 samples). PLSR models with different features were built using calibration sets. Numbers of PLS-PC were determined when the root mean squared error of calibration (RMSEC) reached the minimum value. The robustness of the calibration models generated was tested by leave-one-out cross validation. Considering the predictive ability of models for real samples as well, data in the prediction sets were input

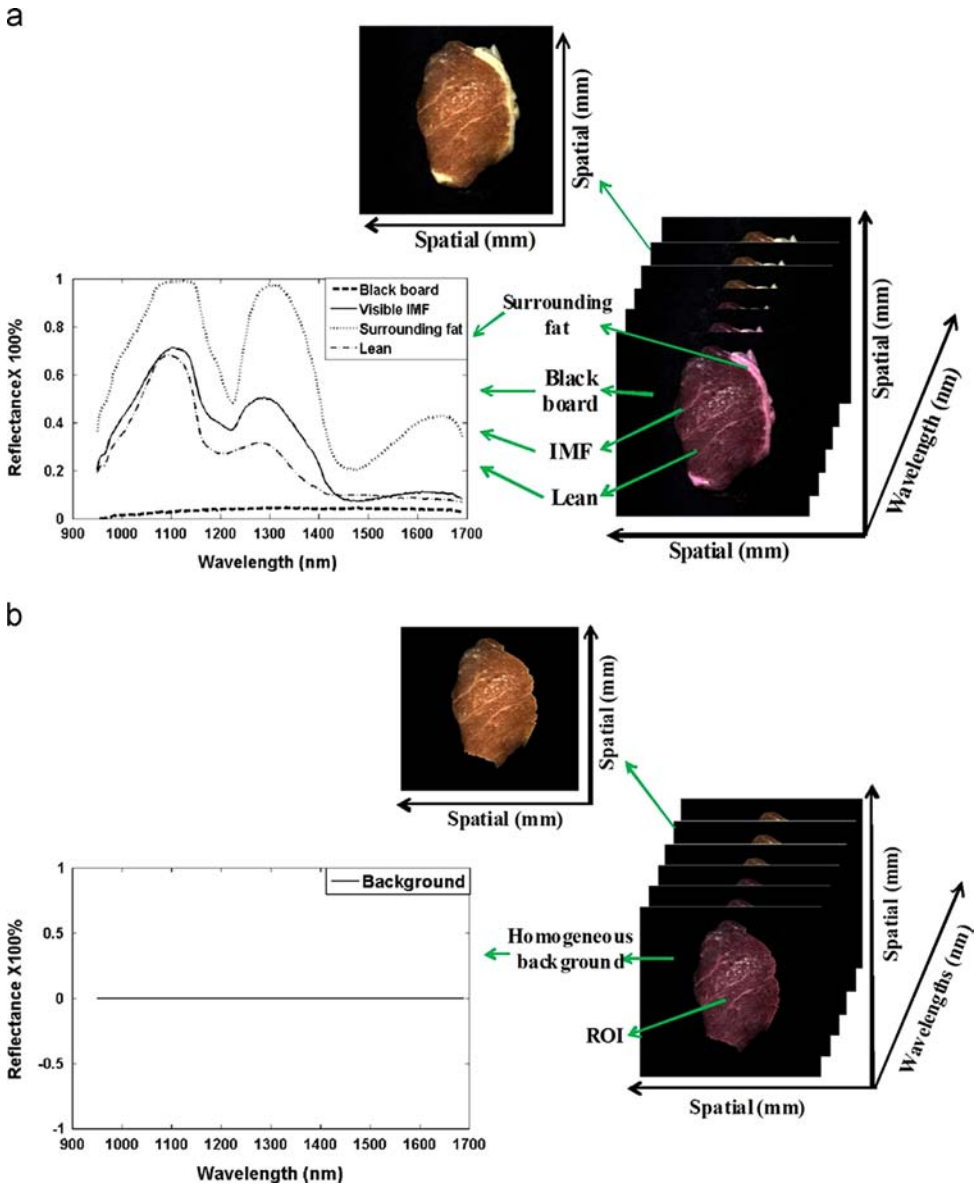

Fig. 3. Construction of *hypercube* and segmentation of ROI. (a) Raw *hypercue*, hyperspectral images, and spectra of black board, visible IMF, surrounding fat, and lean, (b) ROI and spectrum of homogeneous background pixel.

into calibration models for testing. After the numbers of PLS-PC were determined, values of GF-based or GLCM-based models that produced best results were selected along with corresponding optimal parameters of feature extraction. The efficiency of PLSR models was assessed according to following statistical values of calibration sets, cross validation sets, and prediction sets: the correlation coefficient of calibration (*Rc*), cross validation (*Rcv*), and prediction (*Rp*), the root mean square error of calibration (RMSEC), cross validation (RMSECV), and prediction (RMSEP). Models with greater *Rc*, *Rcv*, and *Rp* values, and lower RMSEC, RMSECV, and RMSEP values were preferred.

The most valuable wavelengths for each feature were selected from peaks in their individual plot of regression coefficients. A stepwise procedure was employed to further narrow down the key wavelengths. The variables at selected key wavelengths were input into an MLR model (Eq. (9)), and their performance in calibration, cross validation, and prediction was compared. The most practical model was selected for prediction of IMF content in intact pork.

$$Ym = b_0 + \sum_{i=1}^{i=n} X_i \times b_i \tag{9}$$

where b_0 and b_i are regression coefficients, Ym is the measured IMF content of pork samples,X_i is the variable at the ith wavelength, n represents the number of key wavelengths used, i.e. variables. The

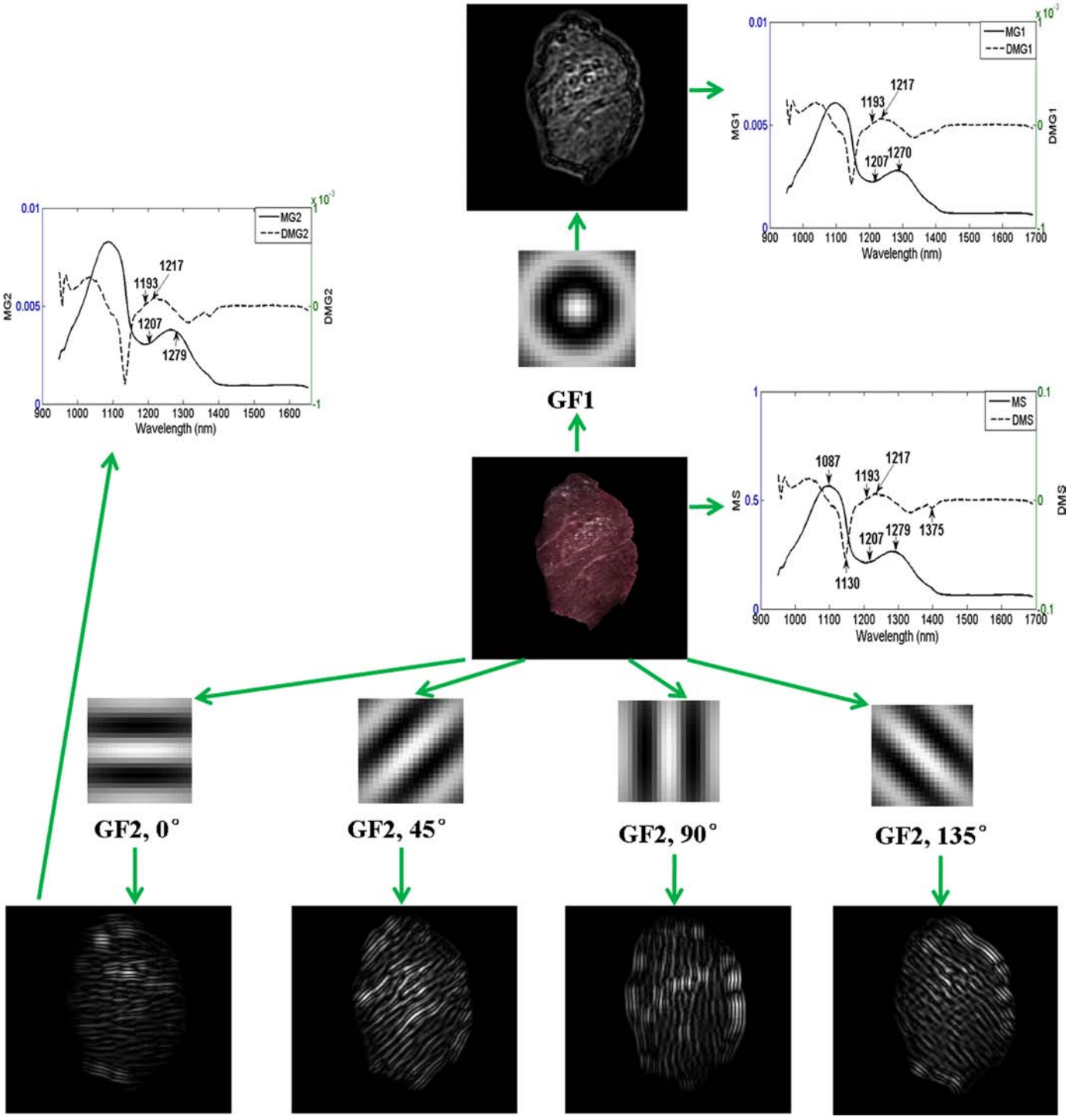

Fig. 4. The raw ROI, GF1, GF2, corresponding Gabor filtered ROI, and generated typical spectral responses.

multiple linear regression model was assessed by statistical values of *Rc*, *Rcv*, *Rp*, RMSEC, RMSECV, and RMSEP. Models with greater *Rc*, *Rcv*, and *Rp* values, lower RMSEC, RMSECV, and RMSEP values, and smaller differences between RMSEC, RMSECV, and RMSEP were preferred.

2.6. Visualization of IMF content in pork by distribution map

Since pork is a heterogeneous material, the visualization of IMF distribution would allow a better interpretation of the IMF content in pork. One advantage of hyperspectral imaging is that it provides spectral information of each pixel in pork image, which means the IMF content of each pixel can be predicted by inputting the spectrum into a prediction model. Furthermore, the spectral information from hyperspectral imaging includes both external information regarding the objects of interest, as well as internal information, making hyperspectral imaging more suitable for prediction of IMF content, as IMF is distributed not just on the surface of pork, but throughout the whole pork sample. Hence, application of hyperspectral imaging has the potential to assist in the visualization of IMF content in intact pork cuts. Towards this purpose, reference data of IMF content of each pixel would be required to build an accurate prediction model. However, it is not possible to measure the IMF content of a pixel. To overcome this challenge, the best and simplest MLR model that was constructed based on mean spectrum or image parameters in previous step was selected. The MLR model was applied to the adopted spectral or image features of each pixel to predict the IMF content of each pixel in the pork image. By showing the pixel-based IMF content, the distribution map of IMF content in pork was then generated. This would help the understanding of IMF distribution in pork and also assist in conducting further detailed study at the pixel level.

3. Results and discussion

3.1. IMF content and ROI of hyperspectral images

A total of 83 pork loin chops were investigated in this study. Wide variations in IMF contents were observed for the total pork cutlets (n=83), calibration set (n=56), and prediction dataset (n=27), with range of 0.51–5.8, 0.51–5.8, and 0.58–3.62, respectively. The range of prediction was covered by calibration set and the standard deviation (STD) of all three datasets was in the same level, ensuring a stable and reliable calibration model.

The conformation of *hypercube* (940–1650 nm) generated by the hyperspectral imaging system and corresponding ROI segmentation are illustrated in Fig. 3(a). A typical NIR image and the spectra of a surrounding fat pixel, an IMF pixel, a lean pixel, and a black board pixel were extracted from a *hypercube*. The reflected spectra of fat and lean showed different scales of intensity but similar features: reflected peak around 1100, 1300, and 1650 nm, and valley around 1250 and 1450 nm. The main constituents of fat and lean include lipid and water, whose peak absorption bands show a great deal of overlapping [28]. Besides, each hyperspectral image was composed of not only the external information of sample, but also the internal information acquired by penetration of NIR spectra into the sample. Since pork is a heterogeneous object, the spectrum from one pixel may contain information of lean and fat in different layers simultaneously. Pork was cut across the grain of muscle cells. Each layer included information of numerous muscle cells. This would explain the similarity in spectral characteristics between lean and fat. The reflectance of a black board pixel was near but not absolutely zero. To screen the board and surrounding fat from the image being analyzed, automatically segmented masks were applied to each NIR image across the waveband of 940–1650 nm, such that reflected values for non-ROI areas were all set to zero. The resultant spectrum of background pixel is absolutely zero in Fig. 3(b).

3.2. Spectra from raw ROI and Gabor filtered ROI and the first derivative of spectra

The raw ROI and the corresponding Gabor filtered ROI (f= 0.1, σ= 10), and typical typical mean spectra of raw ROI (**MS**) and Gabor filtered ROI (**MG1** and **MG2**), and the corresponding responses of first derivative of spectra (**DMS, DMG1** and **DMG2** (θ= 0°)) are illustrated in Fig. 4. ROI in each image was either filtered through the isotropic GF1 or the four orientation GF2 (θ=

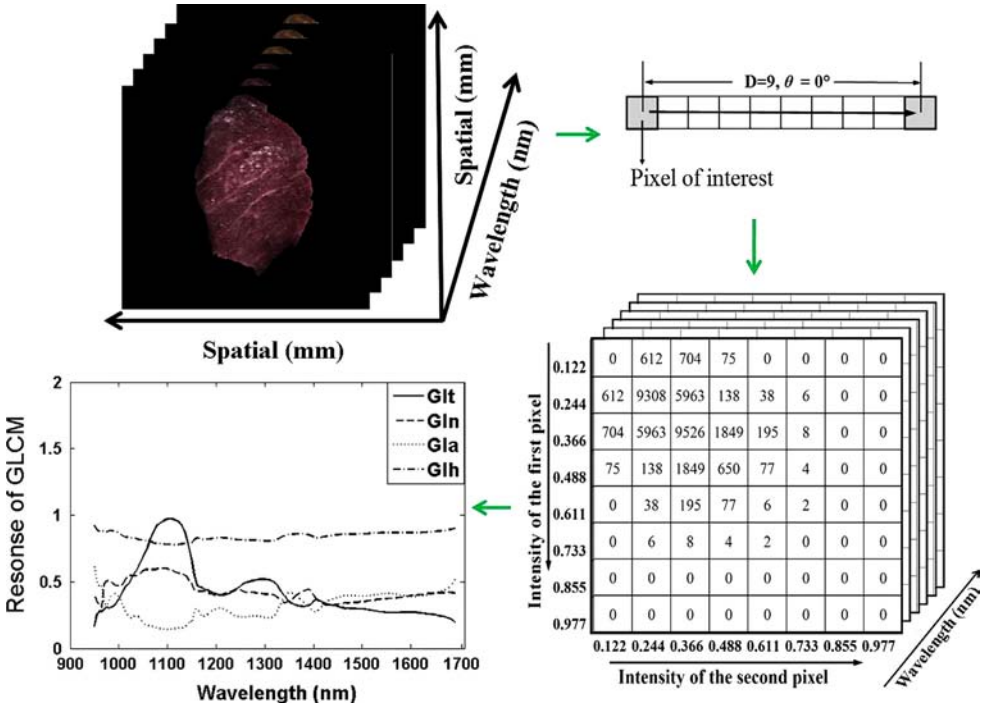

Fig. 5. Formation of GLCM matrix and corresponding texture curves.

Table 1
Results of full waveband-based PLSR models using spectral and texture features.

Features	Parameters			Number of PC	Calibration		Cross validation		Prediction	
	σ	*f*	*θ*		*Rc*	RMSEC	*Rcv*	RMSECV	*Rp*	RMSEP
MS				7	0.90	0.44	0.84	0.55	0.81	0.52
DMS				7	0.90	0.44	0.84	0.55	0.82	0.52
MG1	10	0.1		8	0.90	0.43	0.83	0.56	0.82	0.51
DMG1	10	0.1		7	0.90	0.44	0.83	0.56	0.82	0.52
MG2	10	0.1	0°	7	0.90	0.44	0.85	0.55	0.83	0.52
DMG2	10	0.1	0°	7	0.90	0.44	0.84	0.56	0.82	0.53
	Measurement	*D*	*θ*							
GI	Contrast	9	0°	3	0.80	0.65	0.76	0.70	0.79	0.75

0°, 45°, 90°, 135°). The mean spectra of raw ROI and filtered ROI showed a similar pattern but different magnitudes. All mean spectra showed similar features: a steep peak around 1087 nm, another peak around 1279 nm, and a valley around 1207 nm. The response of first derivative of mean spectra showed similar features: a gradual peak around 1217 nm, and a steep valley around 1130 nm. **MS**, **DMS**, **MG1**, **MG2**, **DMG1,** and **DMG2** spectra of samples were used for multivariate data analysis.

3.3. Texture curve by GLCM

A typical 8-level GLCM matrix of a ROI was formed and the GLCM derived measurements of *contrast*, *correlation*, ASM, and *homogeneity* (**GIt**, **GIn**, **GIa**, and **GIh**) were obtained as illustrated in Fig. 5, where offset distance *D* is 9, and orientation θ is 0°. The minimum reflectance and the maximum reflectance of each ROI were chosen as the lowest and highest levels of GLCM matrix. The range was divided into eight parts, with each portion being regarded as a level. GLCM matrix at each wavelength resulted in a set of four measurements. As depicted in Fig. 5, a GLCM index (**GI**) at continuous wavelengths could be expressed as a curve across 940–1650 nm. Typical curves for **GIt** and **GIn** showed a peak around 1100 nm, similar to features of spectra of **MS** and **MG**. In contrast, **GIh** and **GIa** showed a valley at 1100 nm, indicating that images at this wavelength were less orderly than images at other wavelengths. The highest value of **GIt** at 1100 nm implied a large local intensity variation in the NIR image at 1100 nm. Other peaks around 1300 and 1400 nm were apparent for **GIt** and **GIn** (Fig. 5). Different measurements with different directions and orientations were tried as variables of multivariate data analysis.

3.4. Multivariate data analysis

Features from ROI in calibration set served as input to Eq. (9) and regression matrices (**B**) were obtained. Models were cross validated and tested by independent samples in the prediction set. The results of calibration, cross validation and prediction of all features are listed in Table 1. The optimal parameters of Gabor filters and GLCM were selected based on the performance of PLSR models. When the algorithm-based PLSR models performed the best, the corresponding parameter sets were used as the optimal parameters for the algorithms: $\sigma=$ 10, $f=$ 0.1 for GF1, $\sigma=$ 10, $f=$ 0.1, $\theta=$ 0° for GF2, $D=$9, $\theta=$ 0°, measurement=*contrast* for GLCM. The raw mean spectra and Gabor filtered spectra showed high similarity in PLSR analysis, while **MG2** performed slightly better than the other features. The prediction of IMF content by **GI** was not as strong as mean spectra of raw ROI and Gabor filtered ROI or the first derivative of mean spectra.

Table 2
Optimal wavelengths selected from PLSR models of spectral and texture features.

Features	Optimal wavelengths (nm)
MS	958, 986, 1044, 1116, 1135, 1207, 1279, 1457
DMS	962, 1025, 1116, 1140, 1193, 1217, 1318, 1375
MG1	953, 986, 1044, 1116, 1135, 1207, 1270
DMG1	1025, 1121, 1150, 1193, 1217, 1375
MG2	958, 986, 1044, 1116, 1140, 1207, 1279
DMG2	962, 1025, 1121, 1150, 1193, 1217, 1318, 1375
GIt	1044, 1140, 1174, 1308, 1400

Table 1 shows the regression parameters for models used in selection of optimal wavelengths related to IMF content of pork. Wavelengths corresponding to the first few peak regression coefficients were selected as potential variables, as listed in Table 2. The optimal wavelengths for all the mean spectra were 986, 1044, 1116, and 1207 nm, while the wavelengths of all the first derivative of mean spectra were 1025, 1193, and 1217 nm. Wavelengths of 1044 and 1140 nm were used for GLCM as well as most types of mean spectra. Wavelengths around 960 and 1200 nm were both used as optimal wavelengths for all types of mean spectra and first derivative of mean spectra. Those two wavebands are mainly related to the stretching or deformation vibration of C–H and O–H bonds [28]. The third and second overtones of C–H bonds, which are abundant in fatty acids, resulted absorption

peaks around 930 and 1220 nm [20,28,29]. The frequency around 960 nm, which was derived by stretching vibration of O–H bonds, would be another affect that the band was characterized as an optimal wavelength for all spectral features [20,29,30].

To further lessen the influence of water and lean, a stepwise regression procedure was adopted to simplify the variables at selected wavelengths (Table 2) and further optimize effective wavelengths. The resulting optimal wavelengths, regression coefficients, and results of MLR based on stepwise-selected key wavelengths are listed in Table 3. Only two key wavelengths were selected for almost all of the features except **DMS**, such that the dimension of hyperspectral data was much reduced in comparison to full waveband-based models. Few wavelengths would help the development of an online determination system for IMF content in intact pork. Wavelengths around 1200 nm were adopted by most features except **GIt**. The rare involvement of spectral feature may cause the outline of 1200 nm for texture feature **GIt**, as 1200 nm is closely related to reflected spectra of fat. A limited number of

Table 3
Results of MLR models of spectral and texture features.

Features	Key wavelengths (nm)	Regression coefficient		Calibration		Cross validation		Prediction	
		b_0	b_i	*Rc*	RMSEC	*Rcv*	RMSECV	*Rp*	RMSEP
MS	1207, 1279	0.408	−84.682, 79.259	0.87	0.52	0.86	0.53	0.85	0.55
DMS	1193, 1217, 1375	−0.063	−405.682, 274.427, −144.927	0.88	0.49	0.88	0.50	0.83	0.58
MG1	1207, 1270	0.538	−3030.206, 2740.172	0.87	0.50	0.86	0.51	0.85	0.53
DMG1	1193, 1217	−0.350	−22904.719, 38033.205	0.89	0.44	0.89	0.44	0.86	0.51
MG2	1207, 1279	0.414	−1210.504, 1125.226	0.87	0.51	0.86	0.51	0.85	0.53
DMG2	1193, 1217	0.376	−6034.862, 5736.390	0.88	0.49	0.88	0.49	0.85	0.52
GIt	1140, 1400	0.787	2.779, −2.998	0.82	0.64	0.81	0.65	0.78	0.76

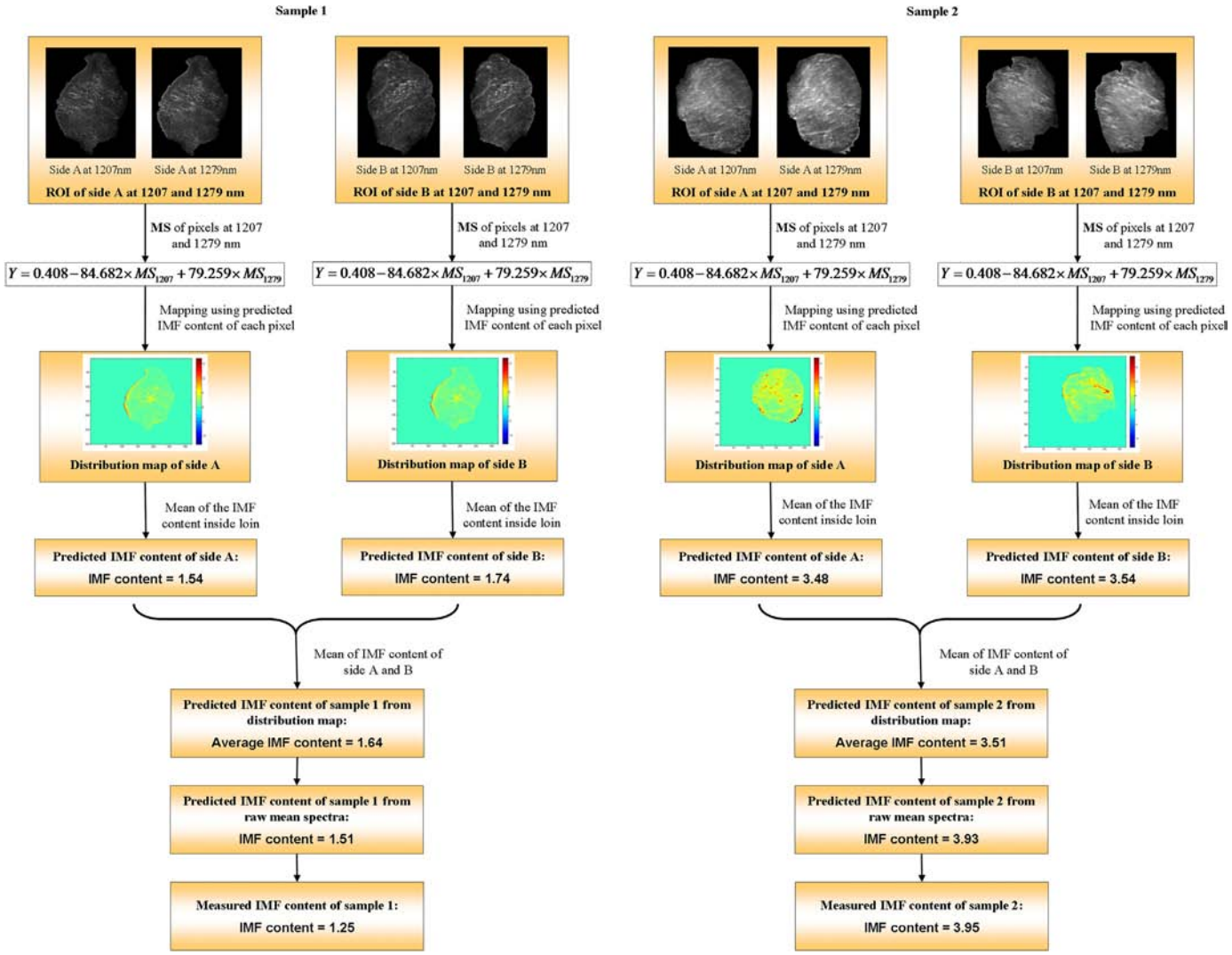

Fig. 6. Visualization of distribution map and the prediction of IMF content of two pork samples.

precise wavelengths would help the development of an effective online determination system for IMF content in intact pork. The performance of key wavelengths-based MLR of **MS, DMS, MG,** and **DMG** was comparable to the performance of full waveband-based PLSR. The **DMG1** produced the best result, with *Rc* of 0.89, *Rcv* of 0.89, and *Rp* of 0.86, using feature **DMG1** at 1193 and 1217 nm. The performance of **GIt** was not as good as the one of other features. However, the MLR model of **GIt** based on key wavelengths outperformed the full waveband-based PLSR model. The further reduction of noise by stepwise analysis may help in data analysis. In this study, a raw mean spectra-based MLR model produced *Rc* of 0.87, *Rcv* of 0.86, and *Rp* of 0.85, using spectra at 1207 and 1279 nm. The prediction results of the raw mean spectra-based MLR model showed that IMF content of both calibration and prediction sets was well predicted. While much fewer wavelengths and less data analysis was involved, these results are comparable to the result of $Rc=0.88$ and $Rp=0.91$ that was reported by Liu et al. [18]. Considering the complexity of application in practice, mean spectra of raw ROI are suggested as the processing technique for IMF content prediction using hyperspectral imaging.

3.5. Visualization of IMF content by distribution map

The MLR model derived from raw mean spectra was used to visualize the distribution of IMF content in pork, by generating both distribution maps of IMF content and the estimated IMF content of pork (Fig. 6). For spectrum of each pixel within a selected ROI, only reflectance at 1207 and 1279 nm was input into MLR model to calculate IMF content of this pixel, i.e. only images at 1207 and 1279 nm were needed for one pork cut. IMF contents of all the pixels inside the ROI yield the distribution map of IMF content. Therefore, the loin portion inside the ROI would affect the profile of the distribution map. Distribution images of two surfaces of one sample were used to generate the predicted IMF content of the sample. Fig. 6 also shows maps of two surfaces of two samples with different measured IMF contents. The ROI of each surface corresponds to one map, showing how IMF content is distributed within the ROI, and in particular, how IMF contents vary drastically between different areas within the same image. In addition, large variation is observed between distribution maps of both sides of a single same sample. The total IMF content of each side (ROI) was generated by averaging the IMF contents of all the pixels within the relative distribution map. The mean of IMF contents of two sides of one sample was used as the predicted IMF content from distribution maps of the sample. The comparison of IMF content of two samples calculated from the raw mean spectrum of ROI, distribution map, and referenced IMF content are depicted in Fig. 6. The error between IMF content from maps and measured values appeared to be slightly larger than the one between IMF content from raw mean spectra and measured values. The prediction model for mapping was built using IMF content measured from the intact pork sample instead of a pixel. Utilization of referenced IMF content from several small portions of the intact pork sample may help to build a more accurate model and therefore enhance the prediction accuracy of the distribution map of IMF content.

4. Conclusions

This study investigated the potential of NIR hyperspectral imaging for non-destructive, fast, and objective assessment of IMF content in intact pork. To mine features from numerous data of spectral images, pattern analysis techniques, i.e. the Gabor filter or the GLCM, were applied. Conventional feature extraction methods, including averaging of spectra and first derivative, were applied as well. Data processing procedure combined by PLSR, stepwise procedure and MLR were used to select effective key wavelengths and establish MLR models. The first derivative of isotropic Gabor filtered mean spectra at 1193 and 1217 nm produced the best result of $Rc=0.89$, $Rcv=0.89$, and $Rp=0.86$. GLCM does not appear to be as effective as Gabor filter and spectral averaging. Considering the feasibility of implementation of such procedures, raw mean spectra are suggested as the most practical feature for prediction of IMF content of intact pork, with little decline in accuracy over the best result by Gabor filter. The wavelengths 1207 nm and 1279 nm were selected as key wavelengths for mean spectra, producing result of $Rc=0.87$, $Rcv=0.86$, and $Rp=0.85$. Distribution map of IMF content using the mean spectra-based MLR model indicated a great potential for detailed IMF inspection in the pork industry.

These promising results demonstrated the great potential of an NIR hyperspectral imaging technique in helping to identify the key wavelengths for IMF content quantification, allowing implementation of a quality assessment component in online inspection systems for intact pork.

Acknowledgments

The authors gratefully acknowledge the Canadian Centre for Swine Improvement Inc. (CCSI) for providing samples.

References

[1] M.S. Brewer, L.G. Zhu, F.K. McKeith, Meat Sci. 59 (2001) 153–163.
[2] E.A. Bryhni, D.V. Byrne, M. Rødbotten, S. Møller, C. Claudi-Magnussen, A. Karlsson, H. Agerhem, M. Johansson, M. Martens, Meat Sci. 65 (2003) 737–748.
[3] J. Brøndum, L. Munck, P. Henckel, A. Karlsson, E. Tornberg, S.B. Engelsen, Meat Sci. 55 (2000) 177–185.
[4] M. Prevolnik, M. Candek-Potokar, D. Skorjanc, S. Velikonja-Bolta, M. Skrlep, T. Znidarsic, D. Babnik, J. Near Infrared Spec. 13 (2005) 77–85.
[5] N. Barlocco, A Vadell, F. Ballesteros, G. Galietta, D. Cozzolino, Anim. Sci. 82 (2006) 111–116.
[6] B. Savenije, G.H. Geesink, J.G.P. Van der Palen, G. Hemke, Meat Sci. 73 (2006) 181–184.
[7] N. Prieto, R. Roehe, P. Lavín, G. Batten, S. Andrés, Meat Sci. 83 (2009) 175–186.
[8] A.A. Gowen, C.P. O'Donnell, P.J. Cullen, G. Downey, J.M. Frias, Trends Food Sci. Technol. 18 (2007) 590–598.
[9] J. Qiao, M.O. Ngadi, N. Wang, C. Gariepy, S.O. Prasher, J. Food Eng. 83 (2007) 10–16.
[10] L. Liu, M.O. Ngadi, S.O. Prasher, C. Gariépy, J. Food Eng. 99 (2010) 284–293.
[11] D. Barbin, G. ElMasry, D.W. Sun, P. Allen, Meat Sci. 90 (2012) 259–268.
[12] D. Barbin, G. ElMasry, D.W. Sun, P. Allen, Anal. Chim. Acta 719 (2012) 30–42.
[13] Y.Z. Feng, D.W. Sun, Talanta 109 (2013) 74–83.
[14] S. Serranti, D. Cesare, F. Marini, G. Bonifazi, Talanta 103 (2013) 276–284.
[15] G. ElMasry, D.W. Sun, Meat quality assessment using a hyperspectral imaging system, in: D.W. Sun (Ed.), Hyperspectral Imaging for Food Quality Analysis and Control, Academic Press/Elsevier, USA, 2010, pp. 273–294.
[16] K. Kobayashi, Y. Matsui, Y. Maebuchi, T. Toyota, S. Nakauchi, J. Near Infrared Spec. 18 (2010) 301–315.
[17] J.P. Wold, M. O'Farrell, M. Hoy, J. Tschudi., Meat Sci. 89 (2011) 317–324.
[18] L. Liu, M.O. Ngadi, S.O. Prasher, C. Gariépy. in: The Institute of Food Technologists (IFT) Annual Meeting & Food Expo. USA (2009).
[19] I. Murray, P.C. Williams, Chemical principles of near-infrared technology, in: P. Williams, K. Norris (Eds.), Near Infrared Technology in the Agricultural and Food Industries, American Association of Cereal Chemists, Inc., St. Paul, Minnesota, USA, 1987, pp. 17–34.
[20] J.S. Shenk, M.O. Westerhaus, J.J. Workman. In: D.A. Burns, E.W. Ciurczak (Eds.), Handbook of Near Infrared Analysis, Practical Spectroscopy Series, New York, USA, 1992, pp. 383–431.
[21] Association of Official Agricultural Chemists (AOAC), Official Methods of Analysis, 15th ed., AOAC, Washington, DC, 1990.
[22] L. Liu, M.O. Ngadi, S.O. Prasher, C. Gariépy, J. Food Eng. 110 (2012) 497–504.
[23] D.A. Clausi, M. Jernigan, Pattern Recogn. 33 (2000) 1835–1849.
[24] L. Ma, T. Tan, Y. Wang, D. Zhang, IEEE Trans. Pattern Recognit. Mach. Intell., 25, 1519–1533.
[25] G. ElMasry, N. Wang, A. El Sayed, M.O. Ngadi, J. Food Eng. 81 (2007) 98–107.
[26] G.K. Naganathan, L.M. Grimes, J. Subbiah, C.R. Calkins, A. Samal, G.E. Meyer, Sens. Instrum. Food Q. Saf. 2 (2008) 178–188.
[27] MJ. Mateo, D.J. O'Callaghan, A.A. Gowen, C.P. O'Donnell, J. Food Eng. 99 (2010) 257–262.

[28] B.G. Osborne, T. Fearn, P.H. Hindle, Applications of near infrared spectroscopy in food and beverage analysis, in: D. Browning (Ed.), Practical NIR Spectroscopy with Applications in Food and Beverage Analysis, Longman Scientific & Technical, London, 1993, pp. 145–159.
[29] J.C. Forrest, E.B. Sheiss, M. Morgan, D.E. Gerrard. Pork quality measurement tools-now and in the future, in: NPPC Pork Quality Summit Proceedings. Des Moines, IA. 1997, pp. 79–96.
[30] L. Bokobza., Origin of near-infrared absorption bands, in: H.W. Siesler, Y. Ozaki, S. Kawata, H.M. Heise (Eds.), Near-Infrared Spectroscopy: Principles, Instruments, Applications, WILEY-VCH Verlag GmbH, Weinheim, Germany, 2008, pp. 11–41.